Adaptive acoustic energy delivery to near and far fields using foldable, tessellated star transducers

2017 Smart Mater. Struct. 26 055021

(http://iopscience.iop.org/0964-1726/26/5/055021)

IOP Publishing Smart Materials and Structures
Smart Mater. Struct. **26** (2017) 055021 (13pp) https://doi.org/10.1088/1361-665X/aa6a93

Adaptive acoustic energy delivery to near and far fields using foldable, tessellated star transducers

Chengzhe Zou and Ryan L Harne

Department of Mechanical and Aerospace Engineering, The Ohio State University, Columbus, OH 43210, United States of America

E-mail: harne.3@osu.edu

Received 12 December 2016, revised 16 March 2017
Accepted for publication 31 March 2017
Published 19 April 2017

Abstract

Methods of guiding acoustic energy arbitrarily through space have long relied on digital controls to meet performance needs. Yet, more recent attention to adaptive structures with unique spatial configurations has motivated mechanical signal processing (MSP) concepts that may not be subjected to the same functional and performance limitations as digital acoustic beamforming counterparts. The periodicity of repeatable structural reconfiguration enabled by origami-inspired tessellated architectures turns attention to foldable platforms as frameworks for MSP development. This research harnesses principles of MSP to study a tessellated, star-shaped acoustic transducer constituent that provides on-demand control of acoustic energy guiding via folding-induced shape reconfiguration. An analytical framework is established to probe the roles of mechanical and acoustic geometry on the far field directivity and near field focusing of sound energy. Following validation by experiments and verification by simulations, parametric studies are undertaken to uncover relations between constituent topology and acoustic energy delivery to arbitrary points in the free field. The adaptations enabled by folding of the star-shaped transducer reveal capability for restricting sound energy to angular regions in the far field while also introducing means to modulate sound energy by three orders-of-magnitude to locations near to the transducer surface. In addition, the modeling philosophy devised here provides a valuable approach to solve general sound radiation problems for foldable, tessellated acoustic transducer constituents of arbitrary geometry.

Keywords: adaptive structure, acoustics, origami, acoustic beamfolding, sound radiation, ultrasonic waves

(Some figures may appear in colour only in the online journal)

1. Introduction

Radiated sound energy can be adaptively guided by multiple acoustic transducers distributed in spatial arrangements and driven with signals having different phase delays and amplitudes [1]. In the far field, i.e. many acoustic wavelengths away from the transducer surface, directivity describes the efficiency that transducers possess to deliver acoustic power into specific angular locations, and it is associated with interference effects pertaining to the transducer geometry and spatial distribution [2]. In contrast, the directivity is not fully developed within a few acoustic wavelengths from the transducer surface [3]. On the other hand, in this near field region, considerable focusing of sound energy is possible via a different constructive interference phenomena than that occurring in the far field, which overcomes the traditional range dependence of acoustic pressure amplitude that decreases with increasing distance from the sound source.

Such guided and concentrated acoustic energies realized by driving arrays of acoustic transducers are used for diverse scientific purposes and applications, including but not limited to sound source localization [4, 5], long-range communication

[6, 7], and medical diagnostics and treatment [8–11]. Beamforming is the real-time signal processing technique often leveraged to achieve the required guidance of acoustic energy, and it is classified into two types based on the origins of the phase and amplitude differences provided to transducers within the array. In digital signal processing (DSP), the amplitude 'shading' and phase delays are numerically computed and sent to appropriate transducers for the sought-after constructive and instructive interferences [12]. Although the performance of DSP practices has been broadly improved in recent decades [13–15], this approach for acoustic wave beamforming has several inherent drawbacks. The drawbacks include computational expense to operate in real-time with adaptive performance, questions of stability for real-time control, and limited portability due to the size and bulk of array implementations respecting frequency bands of interest [16–18].

Contrasting DSP, in mechanical signal processing (MSP) [19] the spatial re-distribution of transducers leads to the change of their distances and orientations to the field point. These small configuration changes result in phase and amplitude differences from the many acoustic waves superposing at the field point, despite the use of the same drive signal provided to each transducer of the array. Consequently, MSP methods can bypass the computation and stability challenges of the digital counterparts, while the lack of associated computational infrastructures enhances portability. Yet, in the face of unlimited possibilities to reconfigure transducers, a question is introduced as to whether there are efficient and effective ways to facilitate the energy-guiding process by array and transducer shape change.

Indeed, the emergence of origami-inspired engineering designs provides a feasible solution to this problem. Origami, the ancient art of paper folding, has attracted abundant attention for its exceptional versatility and adaptable performance when harnessed in the design of structural and material systems [20]. A particularly desirable attribute of origami structure is the foldable topology that can be fluently and repeatedly transformed between two and three dimensions and potentially fold into a volume-less form via flat-foldability [20–22]. In addition, the material properties of origami-based structures can be adjusted to large extent by folding [23–25]. Equipped with such adaptive characteristics, origami has inspired numerous novel applications in resonance tuned RF antennas [26, 27], recoverable and reprogrammable structures [23, 28, 29], bistable and multistable mechanical systems [24, 30, 31], and energy absorption devices [32–34].

Building upon this inspiring framework of engineering design, the authors have recently introduced a concept of acoustic beamfolding, wherein the tessellated surfaces of the Miura-ori origami fold pattern serve as the substrate for acoustic transducers [35, 36]. Acoustic beamfolding therefore is a class of MSP that guides sound energy via the topological reconfiguration of the foldable Miura-ori-inspired arrays. Yet, the attention on the Miura-ori unit cell as the constituent of tessellated arrays limits the shape adaptability elsewhere evident in the literature since the Miura-ori kinematically folds identically as a constituent and array within a two-dimensional plane [21]. Comparatively, the vastness of origami-based tessellations being researched [37] reveals a breadth of multi-dimensional shape change that may be realized, thus suggesting much greater potential for sound energy guiding may be realized by the consideration of other tessellated architectures than merely the Miura-ori. Moreover, the authors previously considered only the opportunities borne out in the sonic frequency range where consideration is often placed on the directiveness of acoustic energy delivery to the far field. Contrasting this attention, when deploying ultrasonic waves, such as for medical diagnostics and treatment, a common need is to focus acoustic energy at strategic points in space, often in the near field of the transducers and arrays. In this perspective, the analysis put forward in the previous works [35, 36] is applicable only for the prediction of sound pressure radiation to points in the acoustic far field. Therefore, a modeling methodology able to characterize both near and far field acoustic energy delivery from tessellated acoustic transducers is needed to begin uncovering opportunities for a more generalized guiding of acoustic energy via foldable, tessellated transducers.

As a consequence of these motivations, this research undertakes a comprehensive advancement to the recent state-of-the-art conception of acoustic beamfolding. In a first step, attention is given to an origami constituent here referred to as the Star [38]. The inward-pointing conformations of the Star constituent due to folding, as shown in figure 1, intuitively introduce opportunities for enhancements to both near and far field acoustic energy delivery, similar to the design of fixed satellite dishes [39]. From figure 1, it is observed that the Star constituent consists of 16 triangular facets, is rotationally symmetric, and may be assembled into numerous array configurations, all of which are features that advance beyond the traditional Miura-ori unit cell [21]. The unfolded square shape of the Star transforms into three-dimensions by folding, although the tessellation is not flat foldable. Along with the focus on this new constituent comes the opportunity to establish new analytical procedures that facilitate prediction of near field sound energy delivery, which was not previously undertaken [35, 36].

Thus, this research gives new attention to the Star tessellation as a foldable acoustic transducer. The following section presents the analytical framework established to characterize near and far field acoustic energy radiation from the driven transducer surfaces. Experimental validation and numerical verifications then demonstrate the accuracy and efficiency of the analytical approach to study the new acoustic tessellation. Then, studies are reported that explore the adaptation of near and far field sound energy generated by the Star. Finally, a summary of this research is provided along with key conclusions.

2. Analytical model formulation

This section describes the development of the analytical framework needed to examine the near and far field acoustic

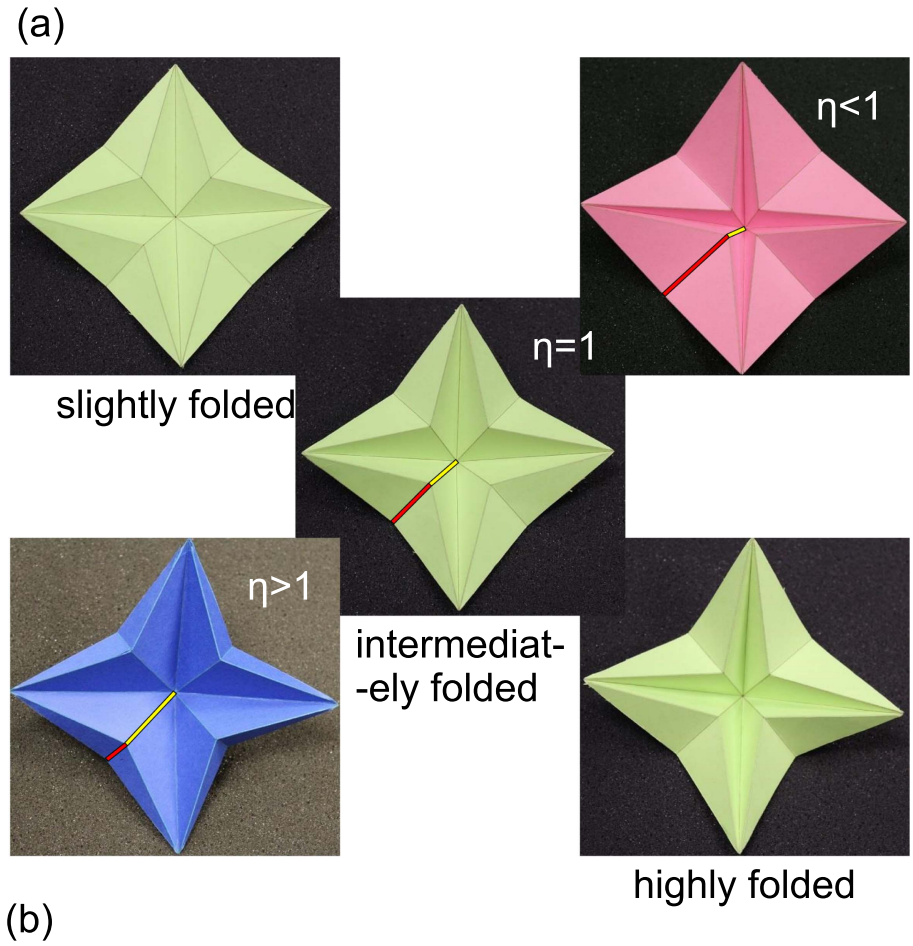

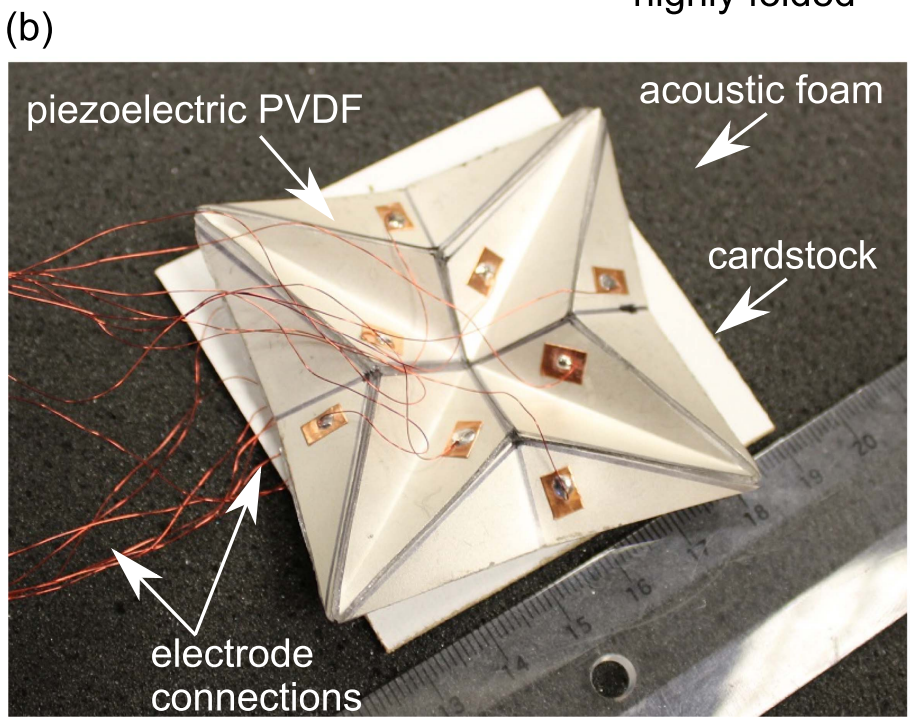

Figure 1. Overview of star-shaped tessellated acoustic transducer. (a) The main diagonal of sub-figures features three folding extents (slightly, intermediately, and highly folded from top left to bottom right) to exemplify the topological changes. The minor diagonal describes three different topologies of Star constituent ($\eta < 1$, $\eta = 1$, and $\eta > 1$ from top right to bottom) when folded intermediately. (b) The Star specimen equipped with surface-bonded, piezoelectric PVDF transducers and electrode connections. The white cardstock below the specimen is used for securing the specimen to the acoustic foam, which collectively emulate no-radiation/baffled conditions for the specimen.

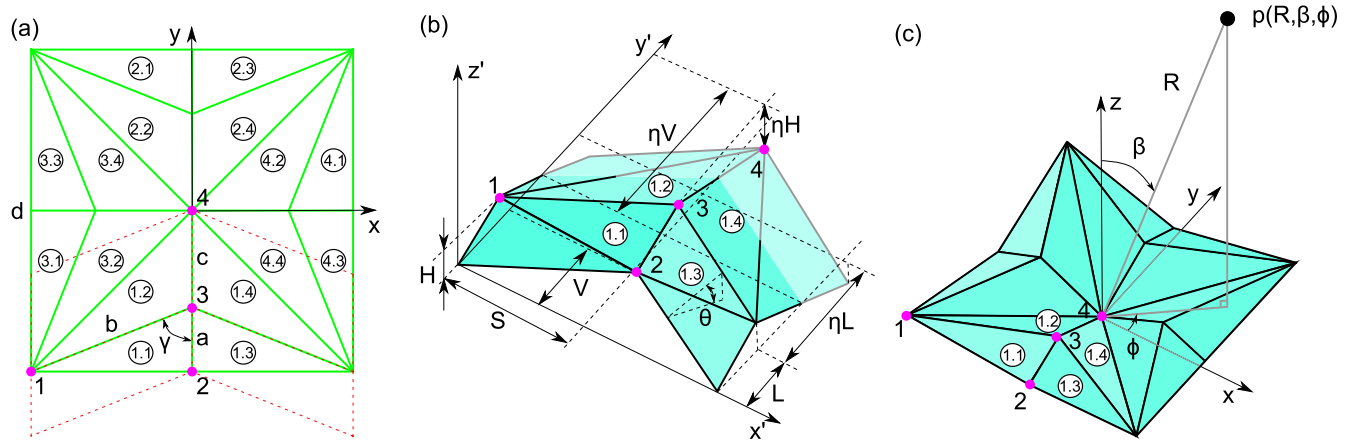

Figure 2. (a) Topology of unfolded Star constituent (solid green lines) and the illustration of its geometrical relations with the unit cell of Miura-ori (dashed red lines). (b) Geometrical notation of folded Miura-ori constituent used to model the three-dimensional geometry of folded Star constituent. (c) Analytical model notation to predict the sound pressure radiated from the Star transducer to the field point $p(R, \beta, \phi)$.

energy radiation from the driven, tessellated facets of the Star constituent. The derivation of the analytical model is based on several assumptions. First, the facets of Star tessellations are rigid, driven transducers such that elastic deformations caused by structural vibration are negligible. Next, the creases between facets are ideal hinges for kinematic folding. Then, the acoustic environment in which the sound radiators are placed is the free field which means there are no echoes and acoustic reflections arriving at the field point for a given frequency under consideration apart from the acoustic waves directly transported from the Star. It is also assumed that the Star is baffled in an infinite plane that permits no propagation of acoustic waves. Finally, the acoustic wave propagation is lossless. All assumptions are effectively satisfied in the experimental undertakings of this research.

2.1. Far field characterization: directive sound

The analytical derivation is composed of geometrical and acoustical modeling, which are intricately coupled by Rayleigh's integral where geometry and acoustics intersect to characterize acoustic wave propagation.

The unfolded Star is shown in figure 2(a). The unfolded, tessellated topology is fully determined by the two variables of edge length d and the length ratio η, where the latter is defined as c/a. All other geometric parameters of the constituent are dependent on these two variables and the relations are described in equation (1). As it pertains to the three-dimensional folded states, the folding angle θ, which is the dihedral angle between facet 1.3 and $x-y$ plane in figure 2(b), is included to specify the influences of kinematic folding.

$$a = \frac{1}{2(\eta+1)}d, \tag{1a}$$

$$b = \frac{\sqrt{\eta^2+2\eta+2}}{2(\eta+1)}d, \tag{1b}$$

$$c = \frac{\eta}{2(\eta+1)}d, \tag{1c}$$

$$\tan\gamma = \eta + 1, \tag{1d}$$

The 16 triangular facets are divided into four groups and numbered in figure 2(a). It is observed that there are only two unique triangular facets among them, while the remaining facets are translated and rotated variants of the two unique shapes. Thus, the unique facets labeled 1.1 and 1.2 in figure 2(a) are considered for the sake of model formulation. The dashed red profile is the topology of unfolded Miura-ori unit cell, and it is seen that facets 1.1 and 1.2 overlap areas of both Star and Miura-ori tessellations. Points 1, 2, 3, and 4 are the shared vertices, as indicated in figure 2(a). The spatial locations of these four vertices in the Miura-ori coordinate system (x', y', z') are expressed using the extents of the folded unit cell of Miura-ori (S, L, H, and V) whose relations are provided in [21] when $\eta = 1$. For the general cases with different η values, the locations are modified based on linear proportionality. For instance, the relative location of point 4 to point 3 in x', y', and z' axes is 0, L, and $-H$, respectively, for $\eta = 1$. For the general case, these values are 0, ηL, and $-\eta H$. Yet, using only the Miura-ori coordinate system, the symmetry of Star topology is not taken advantage of since the Miura-ori system does not possess the rotational symmetry of the Star. Thus, (x', y', z') are here transformed into the Star system (x, y, z) as shown in figure 2(c). Achieving the transformation requires two steps. First, a translation of the current origin is taken to point 4. Second, a rotation of the translated coordinate system is made about the x axis such that the rotation matrix is given in equation (2),

$$\begin{bmatrix} x \\ y \\ z \end{bmatrix} = \begin{bmatrix} 1 & 0 & 0 \\ 0 & \cos\kappa & \sin\kappa \\ 0 & -\sin\kappa & \cos\kappa \end{bmatrix} \begin{bmatrix} x' \\ y' \\ z' \end{bmatrix}, \tag{2}$$

where κ is the rotation angle about the x axis, and counterclockwise direction is positive.

The coordinates of points 1, 2, 3, and 4 in the Miura-ori system are

$$(0,\ L,\ H), \tag{3a}$$
$$(S,\ V,\ 0), \tag{3b}$$
$$(S,\ V+L,\ H), \tag{3c}$$
$$(S,\ V+(\eta+1)L,\ (1-\eta)H). \tag{3d}$$

Once translated to the Star coordinate system, the point locations respectively are

$$(-S,\ -(V+\eta L),\ \eta H), \tag{4a}$$
$$(0,\ -(\eta+1)L,\ (\eta-1)H), \tag{4b}$$
$$(0,\ -\eta L,\ \eta H), \tag{4c}$$
$$(0,0,0). \tag{4d}$$

Using the rotation matrix presented in equation (2), the corresponding coordinates in the Star system are

$$(-S,\ -(V+\eta L)\cos\kappa+\eta H\sin\kappa,\ (V+\eta L)\sin\kappa+\eta H\cos\kappa), \tag{5a}$$
$$(0,\ -(\eta+1)L\cos\kappa+(\eta-1)H\sin\kappa,\ (\eta+1)L\sin\kappa+(\eta-1)H\cos\kappa), \tag{5b}$$
$$(0,\ -\eta L\cos\kappa+\eta H\sin\kappa,\ \eta L\sin\kappa+\eta H\cos\kappa), \tag{5c}$$
$$(0,0,0). \tag{5d}$$

In equation (5), only the rotation angle κ is unknown. From figure 2(c), it is observed that the distances from point 1 to x and y axes should be equal due to symmetry of Star, so that the condition of equation (6) must hold.

$$-(V+\eta L)\cos\kappa+\eta H\sin\kappa=-S. \tag{6}$$

From equation (6), κ is determined and then substituted into equation (5) to obtain the spatial locations of all points that entirely define facets 1.1 and 1.2, along with their respective edges.

Rayleigh's integral is a used to predict the sound pressure radiated into a semi-infinite space above an unmoving baffle from a two-dimensional acoustic source placed in the plane of the baffle [2]. Here each facet is regarded as a uniformly vibrating, baffled piston under a single angular frequency ω of harmonic excitation. Thus, due to the coupling of adjacent fluid particles at the vibrating facets' surface, the radiated pressure to the field point is determined by Rayleigh's integral:

$$p(R,\ \beta,\ \phi,\ t)=\mathrm{j}\frac{\rho_0\omega u_0}{2\pi}\mathrm{e}^{\mathrm{j}\omega t}\int_A\frac{\mathrm{e}^{-\mathrm{j}kr}}{r}\mathrm{d}A. \tag{7}$$

The field point is defined by distance R from the effective source center, elevation angle β and azimuth angle ϕ away from the origin. The density of the fluid medium is $\rho_0=1.104\,\mathrm{kg\,m^{-3}}$ given the current attention to airborne propagation of acoustic waves; A is the surface area of the vibrating facets; u_0 is the amplitude of the normal velocity uniformly distributed over A; $k=\omega/c_0$ is the acoustic wavenumber with the sound speed $c_0=343\,\mathrm{m\,s^{-1}}$; r is the distance from the differential element $\mathrm{d}A$ to the field point.

The Rayleigh's integral of equation (7) can be rewritten [36]

$$p(R,\ \beta,\ \phi,\ t)=\mathrm{j}\frac{\rho_0\omega u_0}{2\pi}\mathrm{e}^{\mathrm{j}\omega t}\frac{\mathrm{e}^{-\mathrm{j}kR}}{R}\int_A\mathrm{e}^{\mathrm{j}(\psi_1x+\psi_2y+\psi_3z)}\mathrm{d}x\mathrm{d}y, \tag{8}$$

where $\psi_1=k\sin\beta\cos\phi$, $\psi_2=k\sin\beta\sin\phi$ and $\psi_3=k\cos\beta$. The integration area A must be obtained to evaluate the integral. Consequently, the area extents of facet 1.1 and 1.2 are respectively defined by equations (9) and (10).

$$\begin{aligned}
&x_{1.1}\in[-S,\ 0]\ y_{1.1,I}(x)\\
&=\left(1+\frac{-(\eta+1)L\cos\kappa+(\eta-1)H\sin\kappa}{S}\right)\\
&\quad\times x_{1.1}-(\eta+1)L\cos\kappa+(\eta-1)H\sin\kappa\\
&y_{1.1,F}(x)=\left(1+\frac{\eta(H\sin\kappa-L\cos\kappa)}{S}\right)x_{1.1}\\
&\quad+\eta(H\sin\kappa-L\cos\kappa)\\
&z_{1.1}(x,\ y)=\frac{1}{L\cos\kappa+H\sin\kappa}\left(-\frac{HV}{S}x_{1.1}\right.\\
&\quad\left.+(H\cos\kappa-L\sin\kappa)y_{1.1}+2\eta HL\right),
\end{aligned} \tag{9}$$

$$\begin{aligned}
&x_{1.2}\in[-S,\ 0]\ y_{1.2,I}(x)=\left(1+\frac{\eta(H\sin\kappa-L\cos\kappa)}{S}\right)x_{1.2}\\
&\quad+\eta(H\sin\kappa-L\cos\kappa)\\
&y_{1.2,F}(x)=x_{1.2};\\
&z_{1.2}(x,\ y)=\frac{1}{L\cos\kappa-H\sin\kappa}\left(\frac{HV}{S}x_{1.2}\right.\\
&\quad\left.+(-H\cos\kappa-L\sin\kappa)y_{1.2}\right).
\end{aligned} \tag{10}$$

The subscripts on y denote I initial and F final limits of integration to be used in equation (11). For example, facet 1.3 and 1.4 are symmetrical to facet 1.1 and 1.2 about the y axis in the Star coordinate system, respectively. As a result, for facets 1.3 and 1.4, the following definitions hold

$$\begin{aligned}
x_{1.3}&=-x_{1.1}\ y_{1.3,I}(x)=y_{1.1,I}(-x)\ y_{1.3,F}(x)\\
&=y_{1.1,F}(-x)\ z_{1.3}(x,\ y)=z_{1.1}(-x,\ y),
\end{aligned} \tag{11}$$

$$\begin{aligned}
x_{1.4}&=-x_{1.2}\ y_{1.4,I}(x)=y_{1.2,I}(-x)\ y_{1.4,F}(x)\\
&=y_{1.2,F}(-x)\ z_{1.4}(x,\ y)=z_{1.2}(-x,\ y).
\end{aligned} \tag{12}$$

The expressions of the other 3 facet groups that are similar to equations (9)–(12) are obtained with comparable ease.

Then the total sound pressure is the summation over all the 16 facets

$$\begin{aligned}
p(R,\ \beta,\ \phi,\ t)&=\mathrm{j}\frac{\rho_0\omega u_0}{2\pi}\mathrm{e}^{\mathrm{j}\omega t}\frac{\mathrm{e}^{-\mathrm{j}kR}}{R}\\
&\times\left\{\sum_{i=1}^{16}\int_{x_i}\int_{y_i}\mathrm{e}^{\mathrm{j}(\psi_1x_i+\psi_2y_i+\psi_3z_i)}\mathrm{d}y\mathrm{d}x\right\}.
\end{aligned} \tag{13}$$

In the far field, the sound pressure level (SPL) is often used to characterize the effective delivery of the acoustic energy to

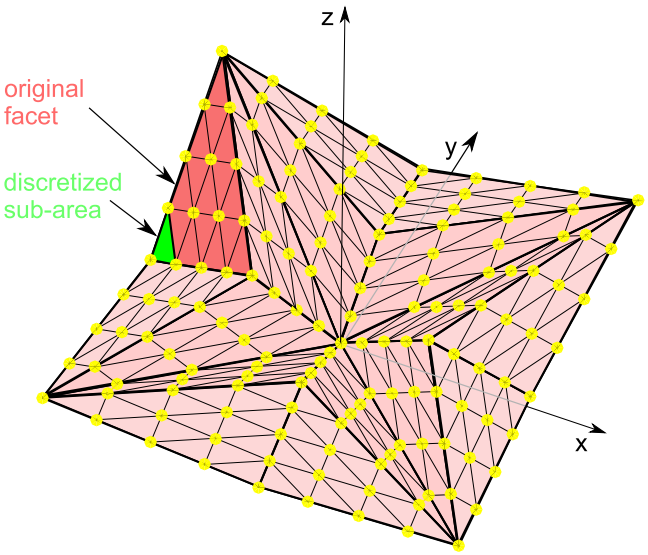

Figure 3. The discretization of the facets into sub-facets for the Star transducer constituent.

different angular locations in space. The SPL is computed by

$$\mathrm{SPL} = 20\log_{10}\left[\frac{p_{\mathrm{rms}}(R,\,\beta,\,\phi,\,t)}{p_{\mathrm{ref}}}\right], \tag{14}$$

where the subscript rms is the root mean square value of p, and p_{ref} is the reference pressure 20 μPa.

2.2. Near field characterization: focusing sound

In section 2.1, the acoustic modeling is derived under far field assumptions. In other words, rays of acoustic waves emanating from the transducer surfaces are presumed to be parallel by the time they arrive at the point in the field where acoustic energy is delivered. Such a modeling approach loses strict applicability in the near field where interference effects are far more nuanced. To characterize the sound energy propagated from the Star constituent transducer into near field regions, this research builds upon the philosophy elaborated in [40] where a vibrating rectangular panel is discretized into sub-areas for sake of predicting near field acoustic radiation from the whole panel. By the discretization of the whole surface into sub-areas, the characteristic lengths of the sub-areas become smaller. In this way, the global near field of the whole transducer is effectively reconstructed by the superposition of local far fields corresponding to each small sub-area. Then, acoustic wave radiation is computed from Rayleigh's integral solved for each sub-area in the far field, while the summation of all sub-area contributions yields a full field response that includes near field wave propagation for the transducer.

Thus, in the following research, the geometry information derived in section 2.1 is utilized and each facet, for instance the dark red triangle in figure 3, is discretized into smaller triangular sub-facets, such as the smaller green triangle emphasized in figure 3. With appropriate refinement of the sub-facet discretization, the near field point of the whole Star transducer falls within the far field for each sub-facet. Then the coordinates of the nodes for sub-facets, as marked by yellow circles in figure 3, are employed to conduct the Rayleigh's integral computations one by one. At last, the total sound pressure response is summed over all the sub-facets. Consequently, the superposed near field sound pressure is

$$p(R,\,\beta,\,\phi,\,t) = \mathrm{j}\frac{\rho_0\omega u_0}{2\pi}\mathrm{e}^{\mathrm{j}\omega t}\left\{\sum_{i=1}^{N}\int_{x_i}\int_{y_i}\frac{\mathrm{e}^{-\mathrm{j}kR_i}\mathrm{e}^{\mathrm{j}(\psi_1 x_i+\psi_2 y_i+\psi_3 z_i)}}{R_i}\mathrm{d}y\mathrm{d}x\right\}, \tag{15}$$

where R_i is the distance from the field point to the center of the ith sub-area, N is the number of the discretized sub-facets. For all results presented in this research, convergence analysis is conducted for the discretization approach to guarantee the efficacy of the theoretical predictions.

3. Experimental validation and numerical verification

To examine the effectiveness of the analytical framework to accurately predict sound energy delivery, this section reports the outcomes of experimental validation and numerical verification efforts.

3.1. Experimental specimen description

Numerous, proof-of-concept experimental specimens are fabricated. One such specimen is shown in figure 1(b). The proof-of-concept Star specimen is assembled from three parts: plastic substrate, piezoelectric materials, and electrode connections. The basic frame of the Star structure is made of polypropylene sheet (Grafix Plastics S16MMPP2024) with thickness 406 μm. The topology of the Star is scored on the plastic sheet using a laser cutter (Full Spectrum Laser H-20 $\times$ 12). The score process decreases the stiffness of the creases significantly, which helps to meet the second assumption in the analytical model formulation regarding purely kinematic folding. For the specimen shown in figure 1(b), the edge length d and length ratio η are 62.5 mm and 1, respectively.

Piezoelectric PVDF film (Measurement Specialties) of thickness 0.11 mm with silver ink electrodes is used to drive the substrate as a transducer to radiate acoustic waves. The PVDF sheet is cut into shapes fitting the profiles of Star facets but with slightly reduced size to prevent electrical shorting between adjacent PVDF. Then, the PVDF films are bonded to the surface of the Star by a thin double-sided tape when the substrate is unfolded. The segmentation of the films is made to ensure that the PVDF is not stretched in the process of folding the Star constituent.

Small copper tape pieces with electrically conductive adhesive are attached to the top and bottom electrodes of each PVDF film. Due to the uniform driving of all PVDF films within the Star constituent, the top electrodes are connected together while the bottom electrodes are likewise connected together, so as to drive the PVDF films in parallel. The resulting, two external leads are subsequently connected to the amplified excitation signal.

3.2. Experimental setup

Far field directivity measurements are taken inside an anechoic chamber. The Star transducer is pinned onto cardstock for sake of maintaining prescribed folded configurations, while the cardstock is then positioned on a bed of acoustic foam. This implementation enables a quasi-baffled state of the specimen since the mounting surface of acoustic foam does not radiate sound. The driving frequencies in the experiments are so high that the structural vibrations of the substrate under the PVDF excitation permit high efficiency acoustic wave propagation, thus avoiding concerns regarding low radiation efficiency of low-order vibration modes of the facets [41].

To measure the acoustic pressure at a field point that is a constant radial distance away from the transducer, a microphone (PCB Piezotronics 130E20) traverses along a hemispherical track of radius 1.168 m and over the elevation angle range $\beta \in [0°, 70°]$, at the azimuth angle $\phi = 0°$. The center of the track is coincident with the center of the radiator. This radial distance sufficiently satisfies the three far field conditions listed in [42] for this specimen and driving frequencies considered in the following cases.

For the experiments, the single frequency exciting signal is created in MATLAB Data Acquisition Toolbox and then sent to the audio power amplifier (AudioSource AMP100). The amplified signal is delivered to an audio output transformer (RadioShack 2731380) and the output voltage is directly used to drive the PVDF films on the Star transducer. Measured sound pressure data are sent to MATLAB for post-processing through signal conditioner (PCB Piezotronics 482C02) and National Instruments data acquisition system (NI 6341). The sampling frequency is 65 536 Hz while the data is digitally filtered with a fourth-order Butterworth filter ranging from 3 to 20 kHz.

3.3. Comparison of experimental and analytical results

The predicted far field SPL by the new analytical formulation is compared with that measured experimentally. In figure 4, each plot presents analytical and experimental results, and the top and bottom row refer to 9 and 13 kHz driving frequencies, respectively. Considering 9 kHz for the unfolded state, a deep node, which refers to significant SPL decrease, appears around the elevation angle $\beta = 40°$, and this feature can be observed analytically and experimentally in figure 4(a). In the experiments, the depth of the node is approximately 20 dB, which means a 100 times power difference exists between the sound energy delivered to broadside ($\beta = 0°$) and that delivered to the angular location $\beta = 40°$. With the increase of folding, as viewed from figures 4(a)–(c), the depth of the node at 9 kHz greatly decreases indicating a less directive propagation of the acoustic energy, while the angular location of the diminished node maintains near to the same elevation angle. These trends are seen in both analytical and experimental results.

At 13 kHz, figure 4(d) shows that two nodes are measured in the experiments for $\theta = 0°$, which is the same number of nodes uncovered by the analytical predictions. The increase of the number of nodes indicates a more directive propagation of sound energy, which is in consistent with the theory of the directivity of multiple transducers [2]. The increased folding is shown to exert large influences on the angular position of the two nodes, while also reducing the depth and significance of each node, similarly observed for the 9 kHz driving frequency. For the 13 kHz waves, considering figures 4(d)–(f) reveals that the node furthest away from broadside moves toward the endfire location ($\beta = 90°$) when the Star constituent is folded more and more. This is not observed experimentally since the node moves beyond the angular measurement range of $\beta \in [0°, 70°]$ while the analysis still suggests the node occurs closer to about $\beta = 83°$.

In the comparisons of analysis and experiment, there are discrepancies that can be explained. The directivity phenomenon results from constructive and destructive interference among waves propagating from the distributed surfaces of transducers. In analysis, the interferences are ideally realized, but the same situation is rarely borne out in experiments of directive responses [43, 44]. Due to the use of small phase differences in order to achieve these directive responses at high frequencies, refined manufacturing capabilities are preferred. For 9 kHz and 13 kHz, the wavelengths are 38.1 mm and 26.4 mm, respectively, which means that the phase differences can vary 9.47° and 13.64° for every 1 mm variation of the spatial distributions of the transducers. Such accuracy is challenging to realize without exceptional fabrication capabilities. Yet, despite such challenges, the experimental results clearly demonstrate the qualitative trends shown through the analysis, such as the number, angular location, and depth of the nodes. Yet, more importantly, the influences of folding on the aforementioned trends observed in the analysis are evident in the data, providing needed experimental validation to the theoretical framework created here.

3.4. Numerical verification method

The boundary element method (BEM) is an important tool for the study of acoustic radiation problems [45]. When dealing with acoustic radiation into a free field, only the boundary of the radiator needs to be meshed with prescribed velocity or pressure boundary conditions (BCs), while the BCs at infinite radial distances from the source are satisfied in the boundary integral equation formulations [46]. One fundamental assumption in BEM is the linearity of the sound field. In the characterization of the Star transducer undertaken here, the SPLs all fall within a linear regime to meet such an assumption. For useful results to be obtained by the BEM approach, at least six linear element edges are required to span the space of the acoustic wavelength under consideration [47]. In the following cases, this basic rule is satisfied. In this work, the openBEM code architecture is utilized in MATLAB [48, 49]. Since the BEM exactly solves the integral equations without recourse to assumptions of the far field, the results obtained by BEM are considered a benchmark for the verification of analytical predictions.

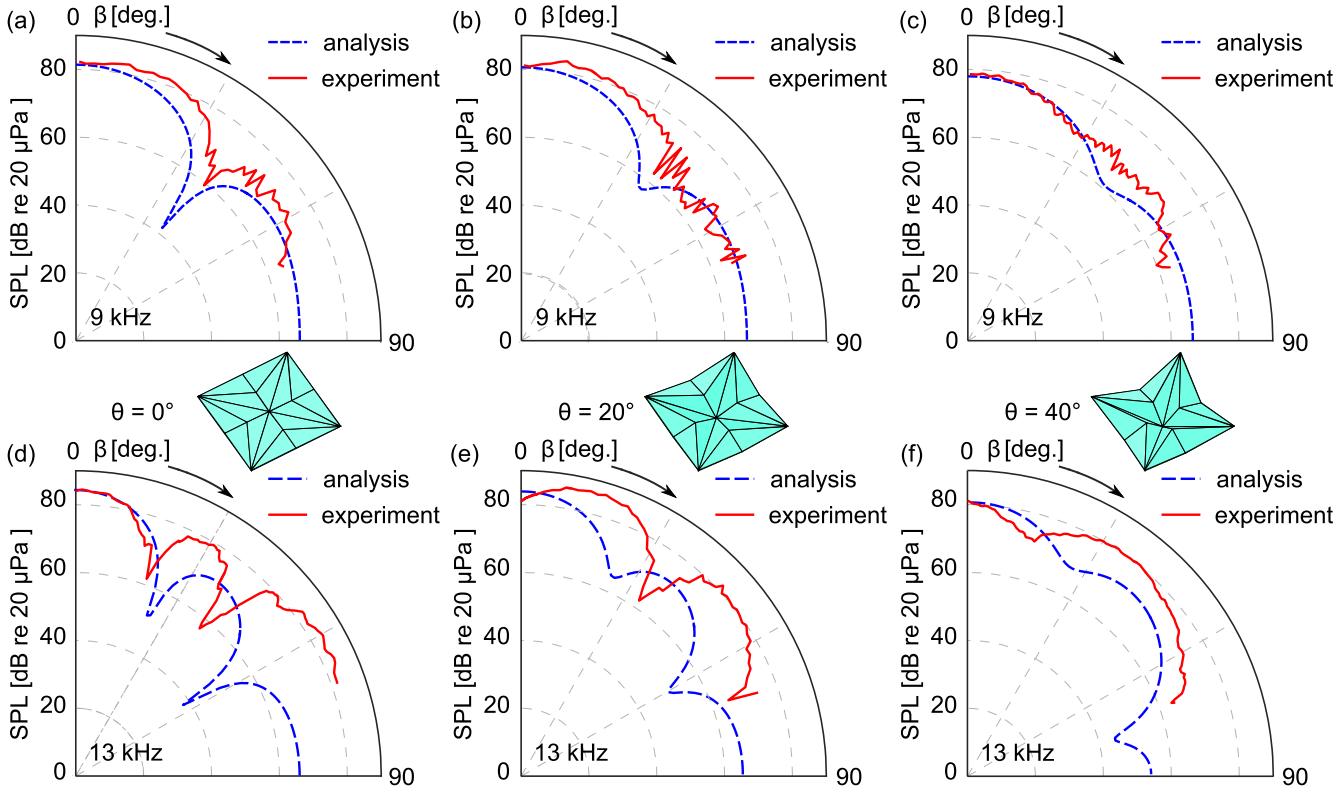

Figure 4. Sound pressure level (SPL) of the Star constituent as a function of the elevation angle β of the field point. Each plot includes the analysis (dashed blue curves) and experiment (solid red curves) results. The driving frequencies are 9 kHz (top row) and 13 kHz (bottom row), respectively. Folding angle $\theta = 0°$ (a), (d), 20° (b), (e), and 40° (c), (f).

3.5. Comparison of numerical and analytical results

Figure 5 presents the comparison of BEM and analytical results for acoustic energy delivery to the far field, to examine the accuracy of the analytical framework. In each case shown throughout figure 5, d and η of the tessellated architecture are 62.5 mm and 1, respectively, which are the same as those measures used in the fabrication of the experimental specimen shown in figure 1(b). The surface normal velocity of the transducer facets is 10 mm s^{-1}. In addition, the distance R is 1.168 m. The ranges of elevation β and azimuth ϕ angles computed are both [0°, 90°]. For the ease of direct comparison, the analysis (left side) and BEM results (right side) are included in one plot for each case. The angular orientation of the azimuthal angle ϕ is thus mirrored between the analytical and BEM data.

Considering the unfolded state driven by 8 kHz in figure 5(a), a deep node exists for each azimuth angle, and the elevation angle of the node is plainly influenced by change in azimuth angle ϕ. For example, when $\phi = 0°$, the elevation angle β of the node is around 45°, while the elevation angle changes to about 90° as the azimuth increases to $\phi = 45°$. Then with the further increase of azimuth angle to 90°, the elevation angle returns to the initial position due to the symmetry of the Star transducer. Such features are observed in both analysis and BEM simulation. As the driving frequency is doubled to 16 kHz as shown in figure 5(d), the transducer becomes more directive and the breadth of each lobe get narrower. There is clear quantitative agreement between the analysis and BEM regarding each of these trends.

Viewing figure 5 from (a)–(c), it can be seen that the SPL of the node gradually increases from 30 to 50 dB when the transducer, excited at 8 kHz, is folded from 0° to 20° to 40°, respectively. This means that the acoustic power difference from the broadside location $\beta = 0°$ to the node can be controlled by folding angle. This attribute is predicted well in analysis when compared to the benchmark BEM results. Similar agreement exists for results shown in figures 5(d)–(f) in regards to the far field SPL at 16 kHz.

For the unfolded state in figures 5(a) and (d), the SPL predicted by the analysis agrees quite well with the BEM simulation results. Yet, discrepancies in the amplitude of the SPL appear between those two approaches when the folding angle θ increases, such as comparing figures 5(a)–(c) at 8 kHz or figures 5(d)–(f) at 16 kHz. These deviations are caused by two aspects. First, the normal directions of folded facets are not parallel like they are when in the unfolded $\theta = 0°$ configuration. This means that reflections can occur, such that the free field assumption is not strictly valid. Secondly, the paths from the transducers to field points can be blocked by other facets when folded, such that acoustic shadows can influence directivity [35]. While BEM takes into account such acoustic phenomena, the analysis must adopt more ideal assumptions for Rayleigh's integral solution that neglect these factors. Nevertheless, as shown by the overall good quantitative and qualitative agreement between the analytical predictions and benchmark BEM

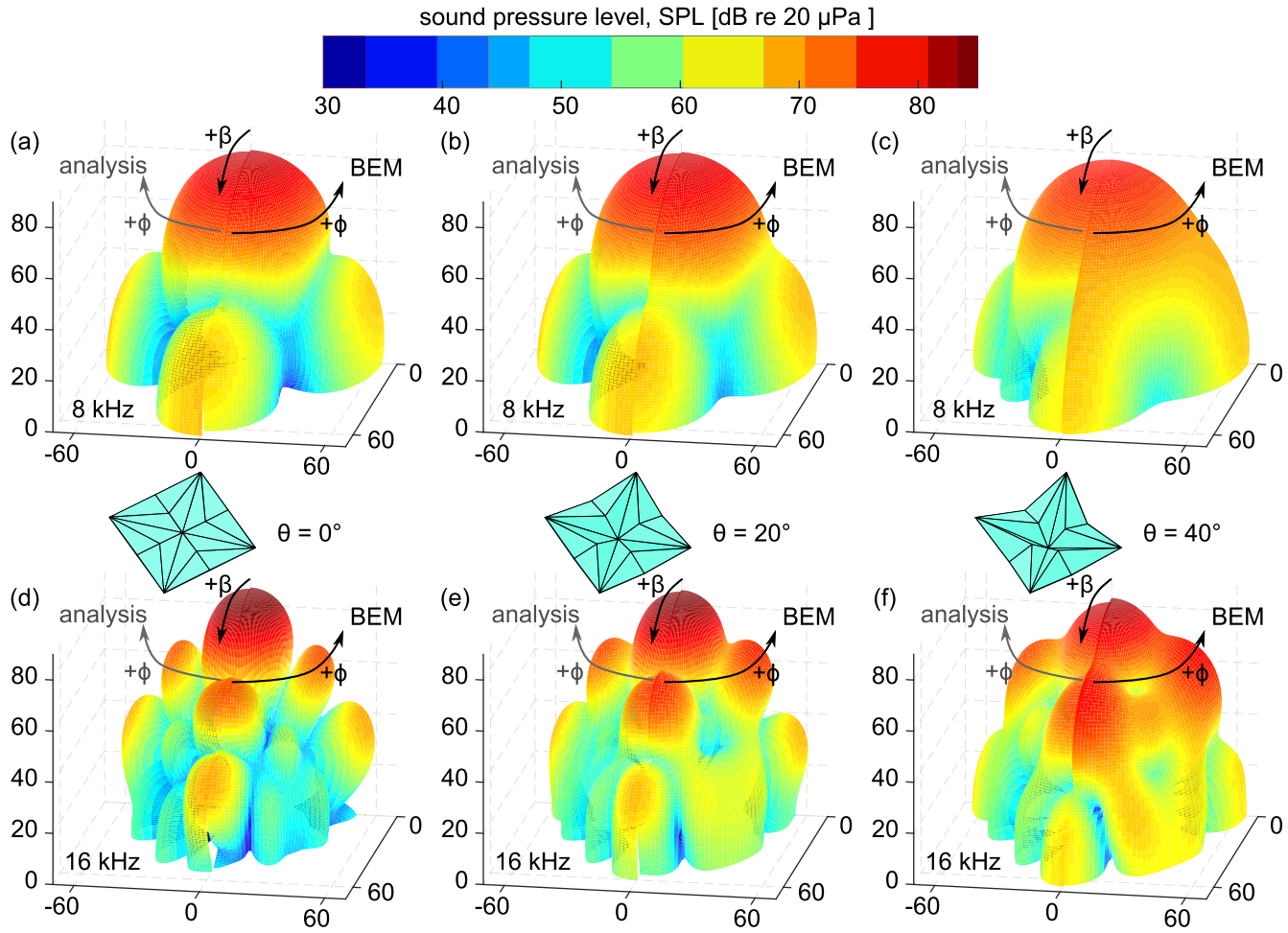

Figure 5. Sound pressure level (SPL) of the Star constituent as a function of the elevation angle β and azimuth angle ϕ of the field point. The spans in x, y, and z axes pertain to SPL and the radial distance from the origin indicates the magnitude of the SPL. Each plot includes the analysis and BEM results. Driving frequency 8 kHz (a)–(c) and 16 kHz (d)–(f). Folding angle $\theta = 0°$ (a), (d), 20° (b), (e), and 40° (c), (f).

simulations, the analysis is still a viable tool to investigate the far field characteristics of the foldable, tessellated Star transducers.

4. Studies and discussions

Following validation by experiments and verification by BEM in section 3, the efficacy of the far field theoretical modeling established in section 2.1 is confirmed. For the near field modeling philosophy described in section 2.2, the acoustic pressure at any arbitrarily located field point is computed as the summation of the far field predictions obtained from sub-facets of the discretized transducer surface. Consequently, the validation by experiments and verification by BEM of the underlying far field prediction strategy provide simultaneous support for the near field predictions obtained by the same model, so long as suitable discretization is provided so that results converge for the specific frequency of interest. Such discretization demands are met in the near field predictions that follow. Thus, for the investigations presented in this section, the model strategies introduced in section 2 are deployed for new insights on opportunities for near field focusing and far field directivity able to be realized by the Star acoustic transducer.

4.1. Influence of tessellation geometry on directive acoustic energy delivery

The most significant characteristic of tessellated origami structures harnessed in this research is the topology change induced by folding. The edge length d and length ratio η entirely determine the geometry of the Star architecture, while the folding angle θ reconfigures the spatial locations of each facet. Based on the non-dimensionality of far field acoustic wave propagation from transducers when considered alongside the acoustic wavenumber k, the only unique geometric feature to consider for the Star constituent is the dimensionless η. Thus, for the following cases studied, d is 62.5 mm while the driving frequency is 16 kHz. This leads to a non-dimensional $kd > 18$ which is well above unity such that strong directionality of acoustic waves in the far field is anticipated [2].

Figure 6 presents analytical predictions of the roles of the length ratio η on the far field directivity of the Star

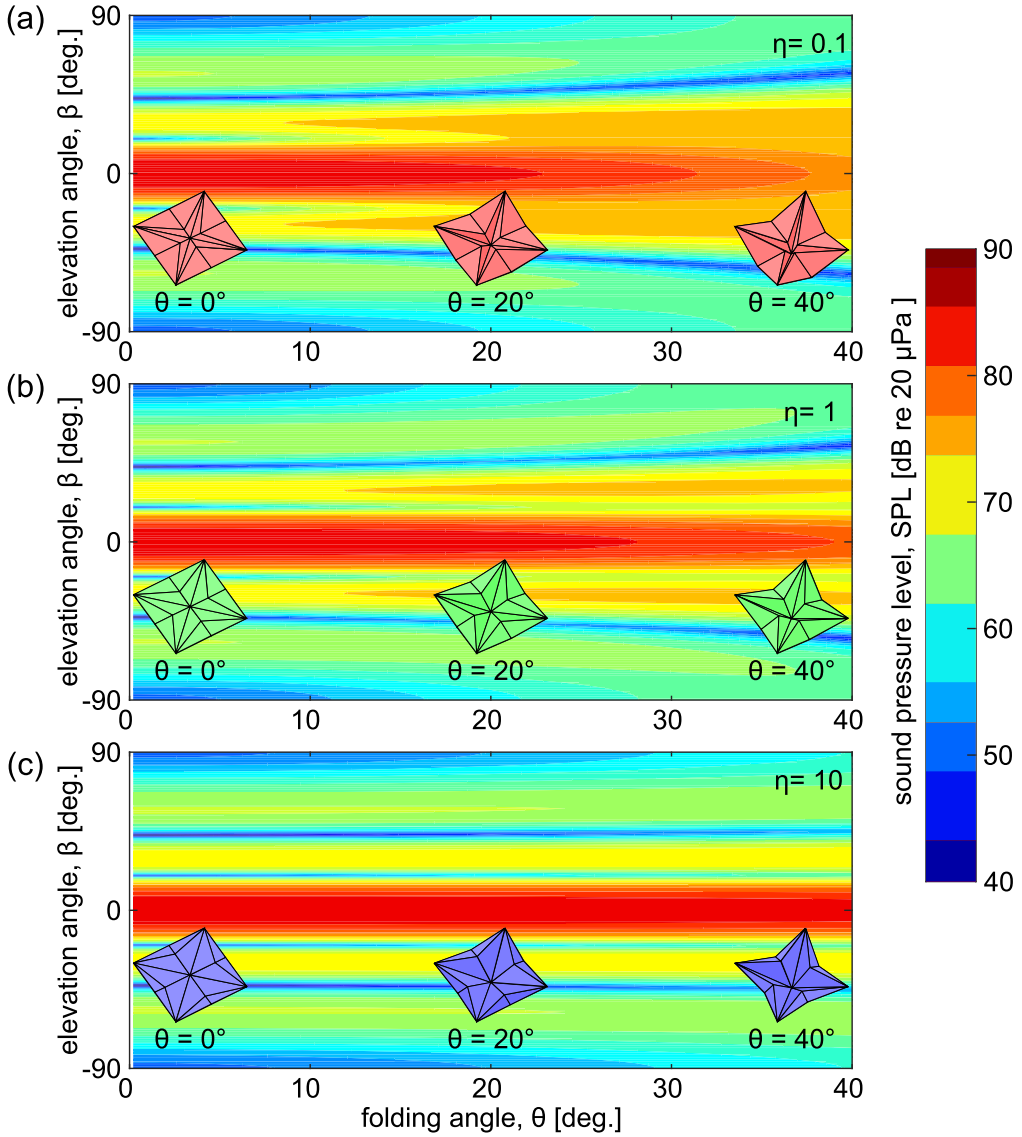

Figure 6. Far field sound pressure level (SPL) of the tessellated acoustic Star transducers as a function of elevation angle β and folding angle θ. Analytical predictions of sound pressure level for length ratio $\eta = 0.1$ (a), 1 (b), and 10 (c). The inset images of the folding Star transducers in (a) and (c) are not reproduced exactly to scale for sake of visual clarity.

constituent. From figure 6(a), considering $\eta = 0.1$ which identifies shorter inner than outer edge lengths, it is found that there are two, unique nodes of acoustic pressure (low SPL) around $\beta = \pm 45°$ when the Star is slightly folded and their elevation angles are increased towards $\beta = \pm 90°$, respectively. The depth of the node nearest to $\beta = \pm 90°$ gradually decreases and then disappears with the increase of folding angle, for all cases of the length ratio η considered in figure 6. Yet, only for length ratios around or less than unity, figures 6(a) and (b), is it found that the major lobe centered on broadside $\beta = 0°$ considerably broadens for increase in the fold angle θ.

Contrasting this trend, for $\eta = 10$ figure 6(c) reveals that the locations in elevation angle of the two nodes near $\beta = \pm 45°$, adjacent to the broadside major lobe, are weakly dependent on the transducer folding. This significantly differs from the influence of folding the Star transducer when the length ratio η is around or less than unity. Thus, the far field sound pressure remains strongly directive for the Star constituent when the geometry consists of large inner edge lengths respecting the outer edge lengths, thus $\eta = 10$. On the other hand, for adaptive directionality of the sound energy, smaller values of the length ratio permit folding-induced change to such characteristics. As a result, the length ratio provides a clear adaptive control of the dependence of the directive response of the tessellated transducers by virtue of the shape change via folding.

Such adaptation is explained intuitively based on the significant topological differences represented by $\eta = 0.1$ and $\eta = 10$. Namely, with the increase of length ratio, a greater proportion of the transducer facets radiate acoustic waves to the far field at broadside considering a given folding angle θ. When the length ratio is large enough, the influence of folding angle on broadside SPL can become negligible so that such

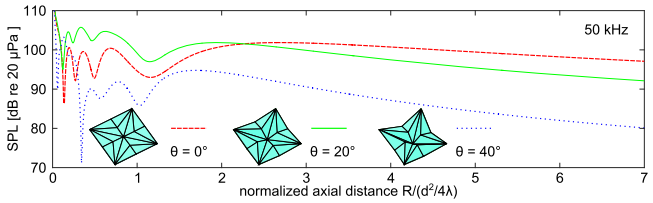

Figure 7. Sound pressure level (SPL) of the tessellated acoustic Star transducers at broadside as a function of normalized axial distance under three folding states ($\theta = 0°$, 20°, and 40°).

influence weakens. Thus, this key non-dimensional parameter of the Star geometry, the length ratio η, permits clear control over folding-induced acoustic energy guiding to the far field.

4.2. Broadside SPL sensitivity induced by axial distance

The adaptive directivity of Star transducers in the far field is shown by the results presented in figure 6. Yet, numerous applications require high sonic or ultrasonic intensities at points in space [8, 9], which necessitates an alternative attention given to energy *focusing* in the strict use of the term. Although specific contexts of acoustic energy focusing require nonlinearities to be accommodated in the theoretical prediction of the resulting acoustic fields, such as for implementation of acoustic radiation force [50] or high-intensity focused ultrasound for thermo-ablative treatment of tumors [51], a vast number of focused acoustic fields are adequately characterized by a linear analysis [8], such as for the large number of medical imaging and diagnostics applications.

Using the analytical framework outlined in section 2.2, figure 7 presents the influences of the axial distance R on the broadside SPL under three different folding angles θ. In the horizontal axis, the radial distance from the specimen R is normalized by the near field-to-far field transition distance of planar square radiators $d^2/4\lambda$ [40], where d is the edge length of the source and λ is the wavelength corresponding to the driving frequency. In this case, d is 62.5 mm and η is 1. At 50 kHz, the acoustic wavelength λ is 6.86 mm. Thus, for points in the horizontal axis of $R/(d^2/4\lambda) \leqslant 1$, the acoustic wave radiation is well within the near field of the Star constituent. For the near field computations, the tessellated transducer surface is discretized into 256 sub-areas to satisfy the local far field conditions. Further discretization is seen to increase computation time but not change the semi-analytical predictions to a meaningful extent. Thus, for the 50 kHz frequency considered here, the discretization to $N = 256$ sub-areas is considered to be sufficient for convergence of results.

The unfolded tessellated transducer, dashed curve in figure 7, reveals a large fluctuation of broadside SPL in the near field, with SPL variation between 80 and 100 dB. Such fluctuations are comparable to those observed for other ultrasonic transducers in the near field [8]. After the transition point, around $R/(d^2/4\lambda) \approx 1$, the fluctuations diminish such that the SPL changes converges towards the established $1/R$ proportionality.

For the Star transducer folded to a partial extent $\theta = 20°$, green solid curve, the amplitudes and locations of the near field

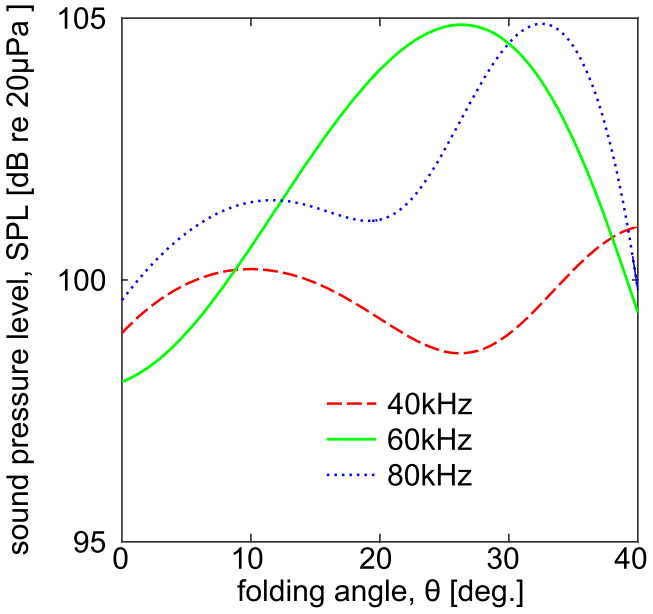

Figure 8. Sound pressure level of the tessellated acoustic transducer at broadside as a function of folding angle for three ultrasonic frequencies, 40, 60, and 80 kHz.

SPL fluctuations are greatly tailored from the unfolded transducer characteristics. Indeed, folding more significantly to $\theta = 40°$, blue dotted curve, reveals further manipulation of the ultrasonic near field focus. For instance, at a normalized axial distance around 0.344, the SPL may be modulated by over 30 dB by the real-time folding of the Star constituent between $\theta = 20°$ to $\theta = 40°$. In other words, sound energy delivery to a point near to the transducer can be modulated by three orders-of-magnitude simply by the mechanical folding of the Star.

4.3. Pumping broadside sound energy in the near field by folding

The near field sound energy focusing capability of Star transducers driven at ultrasonic frequencies is initially revealed by the results shown in figure 7, but the attention to discrete folding angles θ does not comprehensively uncover the acoustic energy pumping empowered by the more common continuous folding of the transducer constituent. In figure 8, the SPL is presented as a function of folding angle θ in order to investigate the role of real-time folding on a point in the near field. Here, d and η are 62.5 mm and 1, respectively, while the axial distance R is 0.02 m. Thus, for the three ultrasonic frequencies considered in figure 8, 40, 60, and 80 kHz, the non-dimensional radial distances $R/(d^2/4\lambda)$ are respectively 0.175, 0.117, and 0.088. The Star transducer is also divided into $N = 256$ sub-facets here, which was likewise the discretization required for the predictions to converge for the frequencies 40, 60, and 80 kHz. For each frequency examined in figure 8, the near field SPL is strongly dependent on the folding. For instance, at 60 and 80 kHz, the SPL is modulated by 6–7 dB by virtue of folding from an angular range of $\theta = 0°$ to around $\theta = 30°$.

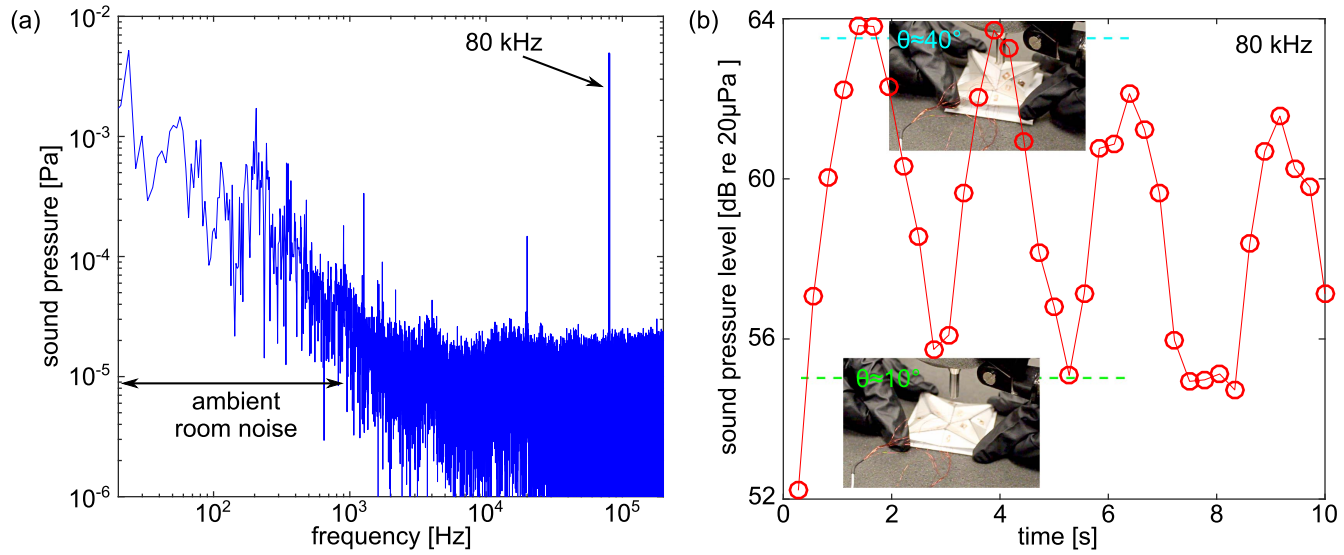

Figure 9. Experimentally recorded near field sound field by topological reconfiguration of Star transducers. The specimen is folded back and forth as illustrated in the insets when it is driven by the 80 kHz harmonic signal. (a) The unfiltered measured sound pressure in frequency domain. (b) The calculated sound pressure level after data is filtered from time domain measurements.

To support the near field analysis results shown in figure 8, experiments are undertaken for the case of 80 kHz excitation. The experiment setup is the same with that described in section 3.2 except that the sampling frequency is increased to 500 kHz. Figure 9(a) shows the level of room noise in comparison to the near field measurement of the 80 kHz tone, to indicate the significant ultrasonic signal delivered by the proof-of-concept Star transducer to the near field microphone. To emulate the analytical variation of folding angle as examined in figure 8, the experiments include folding of the Star between about $\theta = 10^\circ$ to $\theta = 40^\circ$, although the manipulation back and forth between these two configurations is only approximated throughout the undertaking. As shown in figure 9(b), the experiments reveal almost 9 dB of adaptation to the broadside, near field SPL delivered by the Star transducer by virtue of the real-time folding. This modulation extent is similar to the variation of the SPL predicted by the semi-analytical method in figure 7. Such experimental evidence bears out the potential for acoustic beamfolding to empower opportunity for MSP concepts, such as for straightforward and on-demand guiding of ultrasonic acoustic waves via origami-inspired folding principles.

5. Conclusions

This research shows that a method of MSP termed acoustic beamfolding has the potential to enable considerable control of acoustic fields at locations near and far from the foldable transducer surface. These ideas bypass the computation and stability challenges of conventional DSP approaches used to achieve similar functions while moreover introducing new opportunity for compact, portable transducers via the flat-foldability of certain origami-inspired tessellations. In this investigation, the transducer constituent leverages a star-shaped, origami architecture that provides opportunities for both directive acoustic waves and sound energy focusing via its folded configurations. These studies reveal that ultrasonic acoustic energy delivery in air is a prime outlet for the advancements empowered by acoustic beamfolding, while this report introduces a theoretical approach in order to enable the investigation of the opportunities. The modeling strategies detailed here are general tools to predict sound pressure radiation and reception from different tessellated transducers. In other words, by identifying the surface topology of the tessellated surface in three-dimensions, the analytical approach provides means to predict the radiated sound fields at locations near and far from the transducer surfaces, with respect to the acoustic wavelength. Consequently, ongoing studies may leverage the analytical tools established here to examine a wide variety of tessellated acoustic transducers that may find application in various biomedical, communication, and scientific measurement contexts, to name a few.

Acknowledgments

The authors acknowledge Drs P Juhl and V C Henriquez for providing the openBEM code architecture used for BEM computations. RLH acknowledges start-up funds from the Department of Mechanical and Aerospace Engineering at The Ohio State University.

References

[1] Steinberg B D 1976 *Principles of Aperture and Array System Design: Including Random and Adaptive Arrays* (New York: Wiley)
[2] Kinsler L E, Frey A R, Coppens A B and Sanders J V 2000 *Fundamentals of Acoustics* (New York: Wiley)
[3] Bies D A 1976 Uses of anechoic and reverberant rooms for the investigation of noise sources *Noise Control Eng.* **7** 154–63

[4] He T, Pan Q, Liu Y, Liu X and Hu D 2012 Near-field beamforming analysis for acoustic emission source localization *Ultrasonics* **52** 587–92

[5] Chu Z, Yang Y and He Y 2015 Deconvolution for three-dimensional acoustic source identification based on spherical harmonics beamforming *J. Sound Vib.* **344** 484–502

[6] Naguib M and Wiley R H 2001 Estimating the distance to a source of sound: mechanisms and adaptations for long-range communication *Animal Behav.* **62** 825–37

[7] Bolin K, Boué M and Karasalo I 2009 Long range sound propagation over a sea surface *J. Acoust. Soc. Am.* **126** 2191–7

[8] Postema M 2011 *Fundamentals of Medical Ultrasonics* (New York: Spon Press)

[9] Synnevag J, Austeng A and Holm S 2007 Adaptive beamforming applied to medical ultrasound imaging *IEEE Trans. Ultrason. Ferroelectr. Freq. Control* **54** 1606–13

[10] Shahzad A, O'Halloran M, Jones E and Glavin M 2013 Prefiltered beamforming for early-stage breast cancer detection *IEEE Antennas Wireless Propag. Lett.* **12** 500–3

[11] Coussios C C, Farny C H, Ter Haar G and Roy R A 2007 Role of acoustic cavitation in the delivery and monitoring of cancer treatment by high-intensity focused ultrasound (HIFU) *Int. J. Hyperth.* **23** 105–20

[12] Litva J and Lo T K 1996 *Digital Beamforming in Wireless Communications* (Boston: Artech House)

[13] Li J and Stoica P 2005 *Robust Adaptive Beamforming* (New Jersey: Wiley)

[14] Elnashar A, Elnoubi S M and El-Mikati H A 2006 Further study on robust adaptive beamforming with optimum diagonal loading *IEEE Trans. Antennas Propag.* **54** 3647–58

[15] Asl B M and Mahloojifar A 2011 Contrast enhancement and robustness improvement of adaptive ultrasound imaging using forward-backward minimum variance beamforming *IEEE Trans. Ultrason. Ferroelectr. Freq. Control* **58** 858–67

[16] Johnson D H and Dudgeon D E 1993 *Array Signal Processing: Concepts and Techniques* (Englewood Cliffs, NJ: Prentice-Hall)

[17] Schobben D W E 2001 *Real-time Adaptive Concepts in Acoustics: Blind Signal Separation and Multichannel Echo Cancellation* (Dordrecht: Springer)

[18] Jensen J A *et al* 2013 SARUS: a synthetic aperture real-time ultrasound system *IEEE Trans. Ultrason. Ferroelectr. Freq. Control* **60** 1838–52

[19] Turpin J P, Bossard J A, Morgan K L, Werner D H and Werner P L 2014 Reconfigurable and tunable metamaterials: a review of the theory and applications *Int. J. Antennas Propag.* **2014** 429837

[20] Peraza-Hernandez E A, Hartl D J, Malak R J and Lagoudas D C 2014 Origami-inspired active structures: a synthesis and review *Smart Mater. Struct.* **23** 094001

[21] Schenk M and Guest S D 2013 Geometry of Miura-folded metamaterials *Proc. Natl Acad. Sci.* **110** 3276–81

[22] Tolley M T, Felton S M, Miyashita S, Aukes D, Rus D and Wood R J 2014 Self-folding origami: shape memory composites activated by uniform heating *Smart Mater. Struct.* **23** 094006

[23] Silverberg J L *et al* 2014 Using origami design principles to fold reprogrammable mechanical metamaterials *Science* **345** 647–50

[24] Yasuda H and Yang J 2015 Reentrant origami-based metamaterials with negative poisson's ratio and bistability *Phys. Rev. Lett.* **114** 185502

[25] Lv C, Krishnaraju D, Konjevod G, Yu H and Jiang H 2014 Origami based mechanical metamaterials *Sci. Rep.* **4** 5979

[26] Fuchi K *et al* 2016 Spatial tuning of a RF frequency selective surface through origami *Proc. SPIE* **9844** 98440W

[27] Fuchi K, Buskohl P R, Joo J J, Reich G W and Vaia R A 2015 Resonance tuning of RF devices through origami folding *Proc. 20th Int. Conf. on Composite Materials (Copenhagen, Denmark)* pp 1–10

[28] Li S and Wang K W 2015 Fluidic origami: a plant-inspired adaptive structure with shape morphing and stiffness tuning *Smart Mater. Struct.* **24** 105031

[29] Li S, Fang H and Wang K 2016 Recoverable and programmable collapse from folding pressurized origami cellular solids *Phys. Rev. Lett.* **117** 114301

[30] Li S and Wang K W 2015 Fluidic origami with embedded pressure dependent multi-stability: a plant inspired innovation *J. R. Soc. Interface* **12** 20150639

[31] Yasuda H, Chen Z and Yang J 2016 Multitransformable leaf-out origami with bistable behavior *J. Mech. Robot.* **8** 031013

[32] Ma J and You Z 2014 Energy absorption of thin-walled square tubes with a prefolded origami pattern: I. Geometry and numerical simulation *J. Appl. Mech.* **81** 011003

[33] Ma J and You Z 2013 Energy absorption of thin-walled beams with a pre-folded origami pattern *Thin-Walled Struct.* **73** 198–206

[34] Song J, Chen Y and Lu G 2012 Axial crushing of thin-walled structures with origami patterns *Thin-Walled Struct.* **54** 65–71

[35] Harne R L and Lynd D T 2016 Origami acoustics: using principles of folding structural acoustics for simple and large focusing of sound energy *Smart Mater. Struct.* **25** 085031

[36] Lynd D T and Harne R L 2017 Strategies to predict time-harmonic, radiated sound fields from foldable, tessellated, Miura-ori-based transducer arrays for acoustic beamfolding *J. Acoust. Soc. Am.* **141** 480–9

[37] Wang-Iverson P, Lang R J and Yim M (ed) 2011 *Origami 5: Fifth International Meeting of Origami Science, Mathematics, and Education* (Boca Raton, FL: CRC Press)

[38] Jackson P 2011 *Folding Techniques for Designers: From Sheet to Form* (London: Laurence King Publishing)

[39] Miller M J, Vucetic B and Berry L 1993 *Satellite Communications: Mobile and Fixed Services* (New York: Springer Science and Business Media)

[40] Ocheltree K B and Frizzell L A 1989 Sound field calculation for rectangular sources *IEEE Trans. Ultrason. Ferroelectr. Freq. Control* **36** 242–8

[41] Fahy F and Gardonio P 1987 *Sound and Structural Vibration: Radiation, Transmission and Response* (Oxford: Academic)

[42] Bies D A and Hansen C H 2006 *Engineering Noise Control: Theory and Practice* (London: Spon Press)

[43] Sun C, Hirata A, Ohira T and Karmakar N 2004 Fast beamforming of electronically steerable parasitic array radiator antennas: theory and experiment *IEEE Trans. Antennas Propag.* **52** 1819–32

[44] Borg G G *et al* 2000 Plasmas as antennas: theory, experiment and applications *Phys. Plasmas* **7** 2198–202

[45] Atalla N and Sgard F 2015 *Finite Element and Boundary Methods in Structural Acoustics and Vibration* (Boca Raton, FL: CRC Press)

[46] Liu Y 2009 *Fast Multipole Boundary Element Method: Theory and Applications in Engineering* (New York: Cambridge University Press)

[47] Hambric S A, Sung S H and Nefske D J 2016 Engineering Vibroacoustic *Analysis: Methods and Applications* (Chichester: Wiley)

[48] Henriquez V C and Juhl P M 2010 OpenBEM—an open source boundary element method software in acoustics *Proc. Internoise 2010 (Lison, Portugal)* pp 1–10

[49] Juhl P M and Henriquez V C 2015 OpenBEM, Boundary Element Method software (www.openbem.dk)

[50] Marzo A, Seah S A, Drinkwater B W, Sahoo D R, Long B and Subramanian S 2015 Holographic acoustic elements for manipulation of levitated objects *Nat. Commun.* **6** 8661

[51] Kujawska T, Secomski W, Byra M, Postema M and Nowicki A 2017 Annular phased array transducer for preclinical testing of anti-cancer drug efficacy on small animals *Ultrasonics* **76** 92–8